ACS OMEGA

http://pubs.acs.org/journal/acsodf

Article

Enhanced Congo Red Adsorption and Photo-Fenton Oxidation over an Iron-Impeded Geopolymer from Ferruginous Kaolinite: Steric, Energetic, Oxidation, and Synergetic Studies

Esraa R. Adly, Mohamed S. Shaban, Ahmed M. El-Sherbeeny, Wail Al Zoubi,* and Mostafa R. Abukhadra*

Cite This: *ACS Omega* 2022, 7, 31218−31232

Read Online

ACCESS | Metrics & More | Article Recommendations | Supporting Information

ABSTRACT: An iron-impeded geopolymer (Fe/GP) was synthesized from natural ferruginous kaolinite and optical waste for enhanced decontamination of Congo red (CR) dye. The adsorption properties of Fe/GP were assessed using an advanced monolayer equilibrium model of one energy ($R^2 > 0.99$). Fe/GP possessed an active site density of 391.3 mg/g, which induced an adsorption capacity of 634 mg/g at the saturation state. The number of adsorbed CR molecules per site (n = 1.56−1.62) reflected the possible uptake of two molecules per site via a multimolecular mechanism. The adsorption energy (5.12−5.7 kJ/mol) reflected the physical adsorption of the CR molecules via hydrogen bonding and/or van der Waals forces. As a catalyst, notable activity toward photo-Fenton oxidation was achieved even at high CR concentrations. Complete oxidation was observed after 30 (CR concentration: 10 mg/L), 50 (20 mg/L), 80 (30 mg/L), 120 (40 mg/L), and 140 min (50 mg/L). High oxidation efficiency was achieved using 0.1 g/L Fe/GP, 0.1 mL of hydrogen peroxide (H_2O_2), and a visible light source. Increasing the Fe/GP dosage to 0.3 g/L resulted in complete oxidation of CR (100 mg/L) after 220 min. Therefore, synthetic Fe/GP can be used as a low-cost and superior catalyst and adsorbent for the removal of CR-based contaminants via adsorption or advanced oxidation processes.

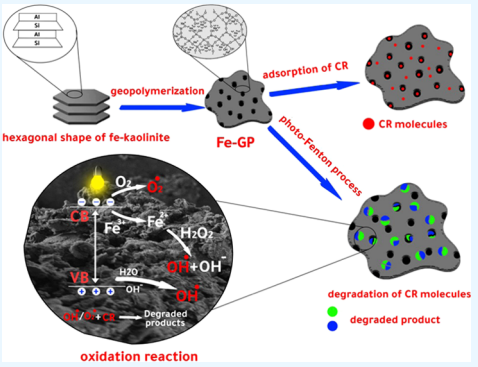

1. INTRODUCTION

Water pollution is the most critical issue that threatens the contemporary world and the safety of the population.[1,2] The World Health Organization (WHO) has raised a critical alarm that 50% of the population of the world will face water scarcity by 2025.[2,3] The quantity of discharged wastewater increases constantly owing to agricultural, industrial, and mining activities and overpopulation.[4] Wastewater contains various inorganic (heavy metals, ammonium, phosphate, nitrate, and sulfate) and organic pollutants (dyes, pharmaceutical residuals, and pesticides). All of the listed chemicals are toxic to humans and other living species and have a detrimental impact on the environment and ecosystem.[5,6] However, among these, synthetic dyes are vital aromatic compounds that are used in several industries. Approximately 10−15% of the produced quantity (7×10^5 tons) is discharged into the surrounding water bodies as untreated and nondegradable industrial wastewater, inducing varying side effects.[7,8]

Among the commonly used dyes, Congo red (CR) is a highly soluble azo dye; it is the sodium salt of benzidinediazo-bis-1-naphthylamine-4-sulfonic acid. CR is widely used in the paper, cosmetics, leather, and textile industries.[5,8] However, the seepage of dissolved CR molecules into water resources induces marked toxicity and environmental effects.[5,8] The presence of CR molecules depletes dissolved oxygen in the water and its distribution during photosynthesis, thereby having a negative impact on the aquatic ecosystem.[9] Moreover, there are several health-related side effects associated with CR pollution, including respiration problems, vomiting, carcinogenic and mutagenic effects, and diarrhea.[10,11] Decontamination of CR molecules from water using innovative and low-cost techniques has been widely conducted;[10,11] adsorption was recommended as an effective removal technique for dissolved dyes owing to its simplicity, high efficiency, recyclability, and low cost.[12,13] Additionally, advanced oxidation processes, including photocatalytic and photo-Fenton oxidation, were reported as being highly effective for dye removal.[14,15] Such advanced oxidation techniques facilitate considerable degradation of dyes and the mineralization of dye molecules into environmental end products in the presence of sunlight or artificial light sources.[5,16] Several factors control the suitability of the adsorbent and catalyst used during the oxidation

Received: June 4, 2022
Accepted: August 16, 2022
Published: August 25, 2022

processes, including recyclability, biodegradability, bandgap energy, recombination rate, thermal stability, safety, fabrication cost, and adsorption capacity.[16]

The development of new structures with enhanced adsorption and advanced oxidation properties based on natural precursors is strongly recommended owing to the cost and environmental considerations.[17] Synthetic geopolymers have been introduced as advanced forms of porous aluminosilicate structures that are widely produced from natural minerals and are used effectively in water remediation applications.[4,18] These polymers possess three-dimensional (3D) network structures of polyalkali aluminosilicate units, which are formed by the condensation reactions of tetrahedral AlO_4 and SiO_4.[19,20] Additionally, they are characterized by marked surface reactivity, a large surface area, ordered porous structures, high organic and inorganic adsorption capacities, and ion exchange properties.[8,20−22] It has been reported that the structure of a typical geopolymer has a dearth of active adsorption sites, which reduces its capacity as an adsorbent; additionally, the polymer contains no active catalytic sites that may be used during the oxidation reactions.[23]

Therefore, several studies have been performed to enhance the properties of geopolymers as adsorbents or catalysts, including metal functionalization and morphological modification.[18,19] The structures of the geopolymers are modified to have more active groups, controlled morphology, controlled pore size distribution, and improved photocatalytic and antimicrobial properties.[24] Additionally, studies have investigated the possible production of effective geopolymer species using low-cost, natural, and easily available precursors, especially incorporated silica and alumina raw materials.[4,8,25] Recently, natural minerals containing metals or enriched with metal impurities have been evaluated as alternative adsorbents or raw materials for the development of other advanced structures.[3] Massive quantities of ferruginous kaolinite are produced annually as the byproducts of mining; such kaolinite has no economic value and its formation during the mining of pure kaolinite increases the hazardous environmental load. Our previous study demonstrated the higher efficiency of ferruginous kaolinite toward the adsorption of dyes than that of fresh kaolinite; this result provides the impetus to modify the properties of ferruginous kaolinite or to incorporate it into advanced materials that exhibit enhanced adsorption and catalytic properties.[3]

Toward this, geopolymers from ferruginous kaolinite were synthesized to form a novel geopolymer structure impeded by structural iron. The structure exhibits enhanced physicochemical properties as an adsorbent with many active receptor sites and is a potential heterogeneous catalyst for the Fenton and photo-Fenton oxidation processes. Based on the previous findings, this study involved the novel synthesis of an Fe-impeded geopolymer (Fe/GP) from natural ferruginous kaolinite and recycled optical glass wastes and verification of its applicability as an enhanced adsorbent and a heterogeneous catalyst for the effective removal of the CR dye. The adsorption properties were evaluated on the basis of experimental variables, classic equilibrium models, and advanced equilibrium studies based on statistical physics theory. The catalytic properties were evaluated by considering the activity of Fe/GP during the photo-Fenton oxidation of the CR dye and based on essential experimental variables in the presence of H_2O_2 and a visible light source.

2. RESULTS AND DISCUSSION

2.1. Characterization of the Carrier. *2.1.1. X-ray diffraction (XRD) Analysis.* The structural transformation of ferruginous kaolinite to a geopolymer was assessed by XRD analysis (Figure 1). The XRD pattern of the raw sample

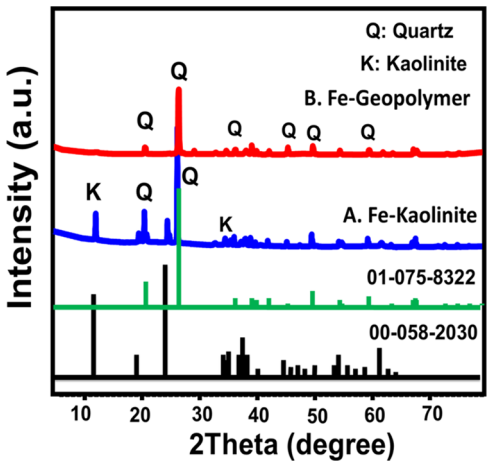

Figure 1. XRD patterns of raw Fe.K (A) and synthetic Fe/GP (B).

demonstrates the existence of well-formed diffraction peaks at 12° (001), 20.88° ($\bar{1}10$), 24.92° (002), and 26.66° (111) (XRD CD No. 00-058-2030) (Figure 1A). These peaks represent crystalline kaolinite minerals, with a structural basal spacing of 7.154 Å.[3] The pattern of the raw sample also shows numerous peaks related to quartz impurities (XRD, CD No. 01-075-8322). After the direct polymerization of Fe-kaolinite to Fe.GP, the identification peaks of kaolinite disappear from the XRD pattern, reflecting the amorphization of its crystalline phases (Figure 1B). The detected phases are related only to quartz impurities, which are highly stable. However, the detection of the main quartz peak at the shifted position (26.8°), in relation to that of the original system (26.66°), reflects the impact of the alkaline conditions on the structure (Figure 1B). This result is supported by the measured microstrain of the quartz phase in the geopolymer (0.179%), which is higher than the detected value for quartz in raw kaolinite (0.077%). Additionally, the crystallite size is markedly reduced from 21.6 to ∼9.2 nm after the geopolymerization process.

2.1.2. Fourier Transform Infrared (FT-IR) Spectroscopy. The FT-IR spectra of both Fe.K and Fe/GP are presented in Figure 2. The FT-IR spectrum of the raw ferruginous kaolinite sample shows peaks ascribed to structural Si−OH (3689 cm^{-1}) and Al−OH (3622 and 912 cm^{-1}); OH bending of adsorbed water (1641 cm^{-1}); and Si−O−Si (1020 cm^{-1}), Si−O−Al (685 and 534 cm^{-1}), and Si−O (456 and 784 cm^{-1}) groups (Figure 2A).[3,26] The peaks in the Fe/GP spectrum are notably shifted from those in the previously reported kaolinite absorption spectra (Figure 2B). The shift might be related to the amorphization of Fe.K during the alkaline conversion and polycondensation of the kaolinite flakes to aluminosilicate gel. Studies have suggested that the marked difference is caused by the reincorporation of impeded Fe ions, as chemical modifiers, into the geopolymer framework.[27] The bands that are detected in the FT-IR spectrum of synthetic Fe/GP are related to structural Si−OH (3696 cm^{-1}) and Al−OH (3654 and 916 cm^{-1}); OH bending of adsorbed water (1627 cm^{-1}); and Si−

https://doi.org/10.1021/acsomega.2c03365
ACS Omega 2022, 7, 31218−31232

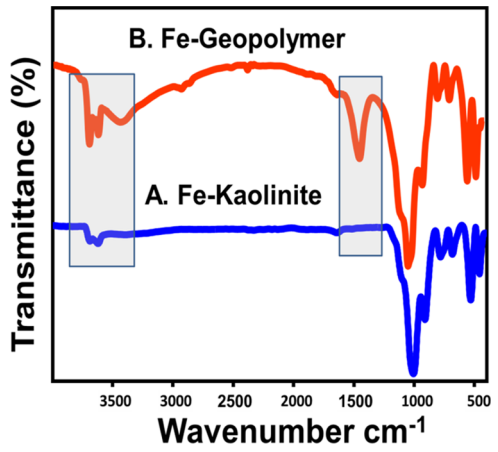

Figure 2. FT-IR spectra of raw Fe.K (A) and synthetic Fe/GP (B).

O−Si (1036 cm^{-1}), Si−O−Al (690 and 540 cm^{-1}), and Si−O (468 and 789 cm^{-1}) groups (Figure 2B).[28,29] The increase in both the intensity and broadness of the peaks corresponding to structural −OH groups indicates that the hydration properties and concentration of the active hydroxyl groups have increased on the surface of the structure (Figure 2B). Additionally, a new band is identified at 1440 cm^{-1}, which corresponds to the bending vibration of the bonded H−O−H molecules trapped within the geopolymer matrix (Figure 2B).[27,28]

2.1.3. Scanning Electron Microscopy (SEM). The obtained SEM images demonstrate the successful polymerization of the kaolinite flakes into the geopolymer (Figure 3). The well-known pseudohexagonal flakes of kaolinite (Figure 3A) are completely converted into massive particles with irregular morphology and rugged topography, which are the commonly observed morphologies of a synthetic geopolymer (Figure 3B). The high-magnification images of the surface of the Fe/GP particles reflect the high porosity of the synthetic Fe-impeded geopolymer particles. Three types of pores can be recognized from the SEM images. The first type is known as the micropores, which can be identified as vesicular pores or vugs and are related to the release and escape of the entrapped gases during the polymerization and drying steps (Figure 3C). The second type is known as the nanopores, which can be identified as structural pores that are related to the matrix of the polymerized alumina and silica units (Figure 3D). The third type is known as the surficial pores, which might be related to the etching effect of the alkaline solutions used during the polymerization step on the kaolinite surface; the surficial pores may possess an aluminosilicate structure or may be formed via the partial dissolution of the optical glass used during the reactions (Figure 3E). These morphological features have a strong impact on the pore volume (0.042 cm^3/g), average pore diameter (8.2 nm), and surface area (103.6 m^2/g) of synthetic Fe/GP.

The results of the EDX spectroscopy of the samples, based on the SEM images, agree with those of FT-IR spectroscopy and XRD analysis (Figure 3F). The spectrum of the raw Fe.K sample demonstrates the existence of the essential kaolinite elements, including O (45%), Si (24.3%), Al (22.3%), and K (2.8%), in addition to iron impurities (5.6%) (Figure 3F). The EDX spectrum of Fe/GP demonstrates an increase in the Si (26.3%), O (48.2%), and Na (9.5%) contents. Additionally, there is an observable decrease in the Al (12.4%) content (Figure 3F). This elemental composition indicates that a geopolymer with a poly(sialate-siloxy)-type Si/Al ratio has formed.

2.2. Adsorption Studies. *2.2.1. Effect of pH.* The solution pH is a key factor during the adsorption of dissolved chemical compounds onto the surface of the solid particles. The pH (2−

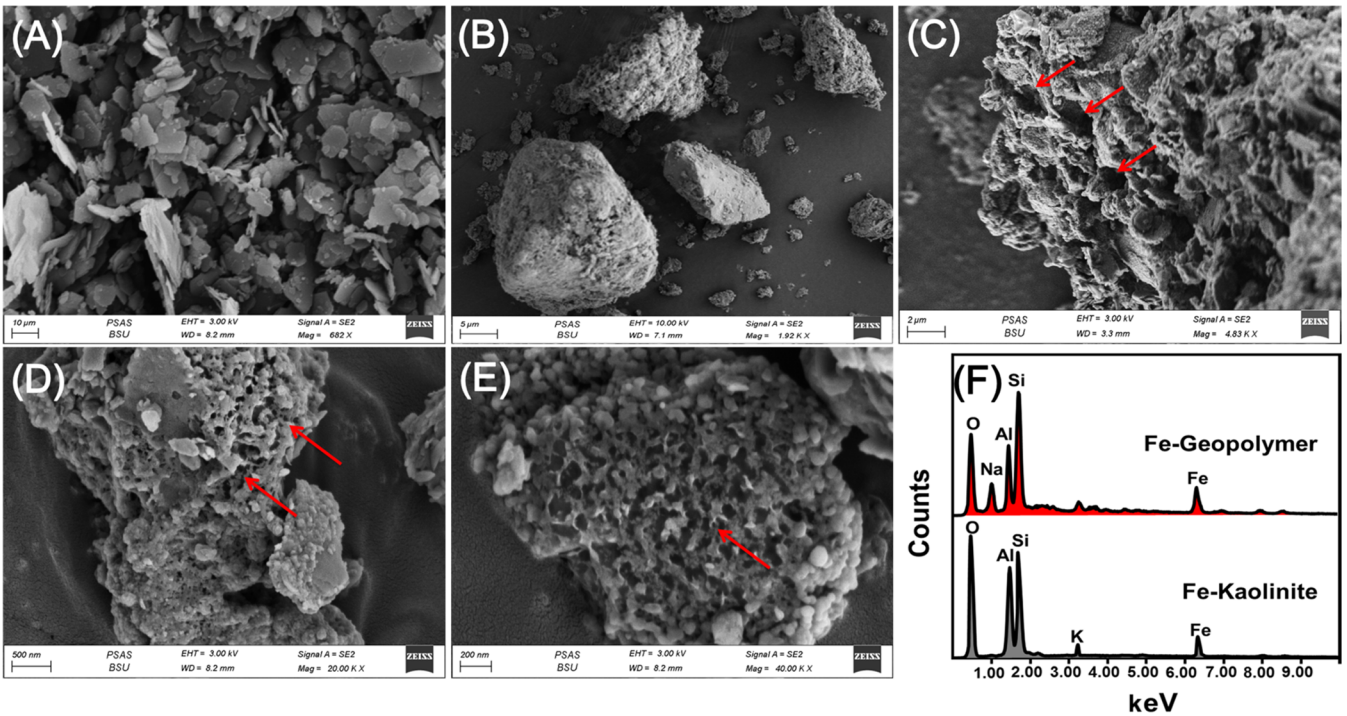

Figure 3. SEM image of the used raw Fe.K (A), general SEM image of the synthetic Fe/GP (B), high-magnification image for the surfaces of the synthetic Fe/GP particles (C, D, E), and EDX spectra of both Fe.K and Fe/GP (F).

https://doi.org/10.1021/acsomega.2c03365
ACS Omega 2022, 7, 31218−31232

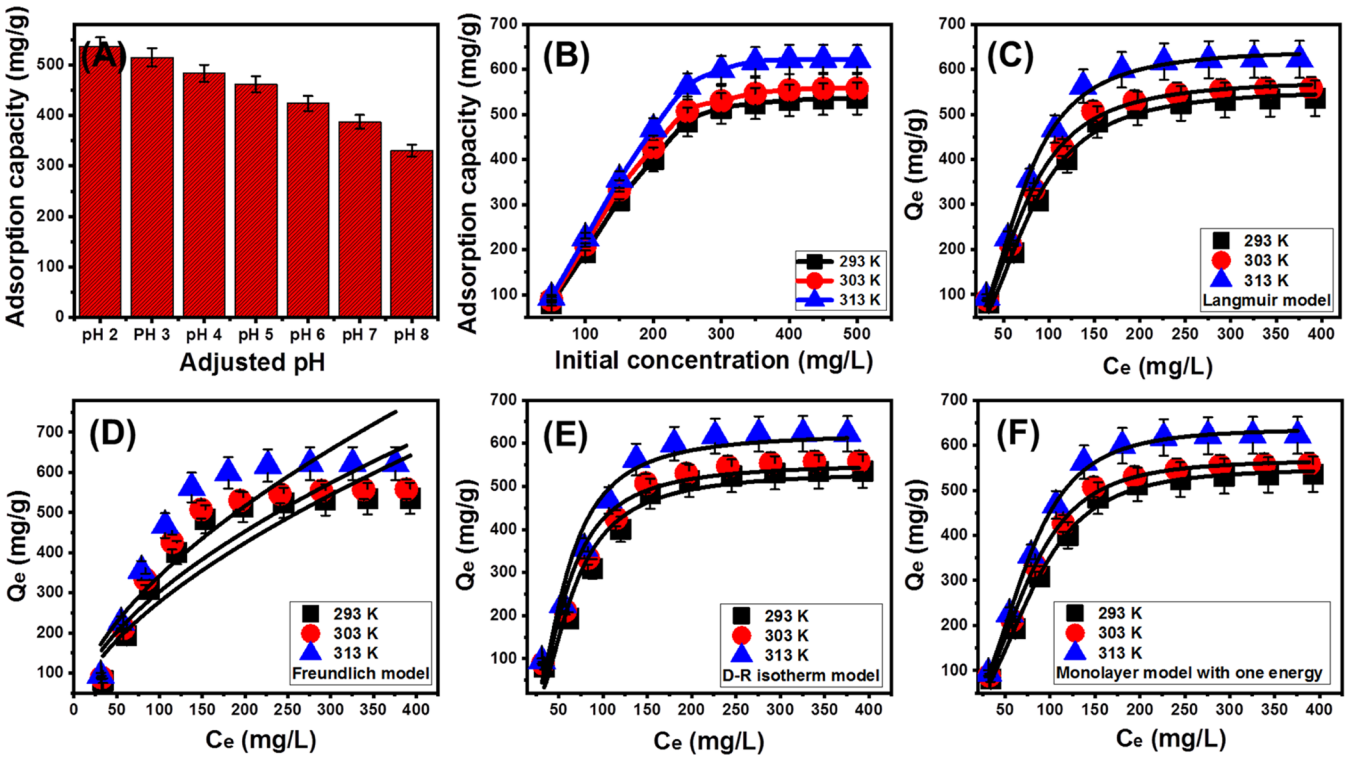

Figure 4. Effect of the solution pH on the uptake of CR dye by Fe/GP (A), effect of the CR concentrations on the uptake capacity of Fe/GP (B), fitting of the CR uptake results with the Langmuir model (C), fitting of the CR uptake results with the Freundlich model (D), fitting of the CR uptake results with the D−R model (E), and fitting of the CR uptake results with the monolayer model of one energy (F).

Table 1. Estimated Mathematical Parameters of the Studied Classic and Advanced Equilibrium Models

			293 K	303 K	313 K
		Parameters of the Classic Isotherm Models			
Fe/GP	Langmuir model	Q_{max} (mg/g)	555.3	575.9	644.12
		b (L/mg)	2.6×10^{-5}	4.16×10^{-5}	2.73×10^{-5}
		R^2	0.98	0.99	0.98
		X^2	0.23	0.163	0.211
	Freundlich model	$1/n$	0.612	0.58	0.59
		k_F (mg/g)	16.5	20.8	22.2
		R^2	0.87	0.86	0.86
		X^2	7.2	8.3	8.72
	D−R model	β (mol^2/kJ^2)	0.1325	0.108	0.107
		Q_m (mg/g)	534.5	552.8	623.5
		R^2	0.95	0.96	0.96
		X^2	2.6	2.11	2.74
		E (kJ/mol)	1.94	2.14	2.15
		Steric and Energetic Parameters of the Advanced Isotherm Model			
Fe/GP		R^2	0.998	0.999	0.998
		X^2	0.187	0.098	0.177
		n	1.56	1.58	1.62
		N_m (mg/g)	345.07	359.6	634.02
		Q_{Sat} (mg/g)	538.3	568.2	129.03
		$C_{1/2}$ (mg/L)	121.86	111.5	107.9
		ΔE (kJ/mol)	5.12	5.52	5.79

8) of the CR solutions was assessed as an experimental variable. The other variables were kept constant [volume, 100 mL; solid dosage, 0.1 g/L; concentration, 500 mg/L; contact interval, 24 h; temperature, 293 K] during the experiments (Figure 4A). The CR uptake results validate the marked decline in the actual capacity of Fe/GP when the pH of the solution changes from 2 (535.6 mg/g) to 8 (330.3 mg/g) (Figure 4A). When the pH of the solutions increases, the negatively charged hydroxyl groups generated on the surface of the Fe/GP particles, during their deprotonation in the alkaline environment, are notably electrostatically repulsed by the negatively charged CR molecules.[30,31] This behavior validates the estimated value of $pH_{(zpc)}$, based on the determined ζ potential values, at different pH levels. The measured $pH_{(zpc)}$ of

https://doi.org/10.1021/acsomega.2c03365
ACS Omega 2022, 7, 31218−31232

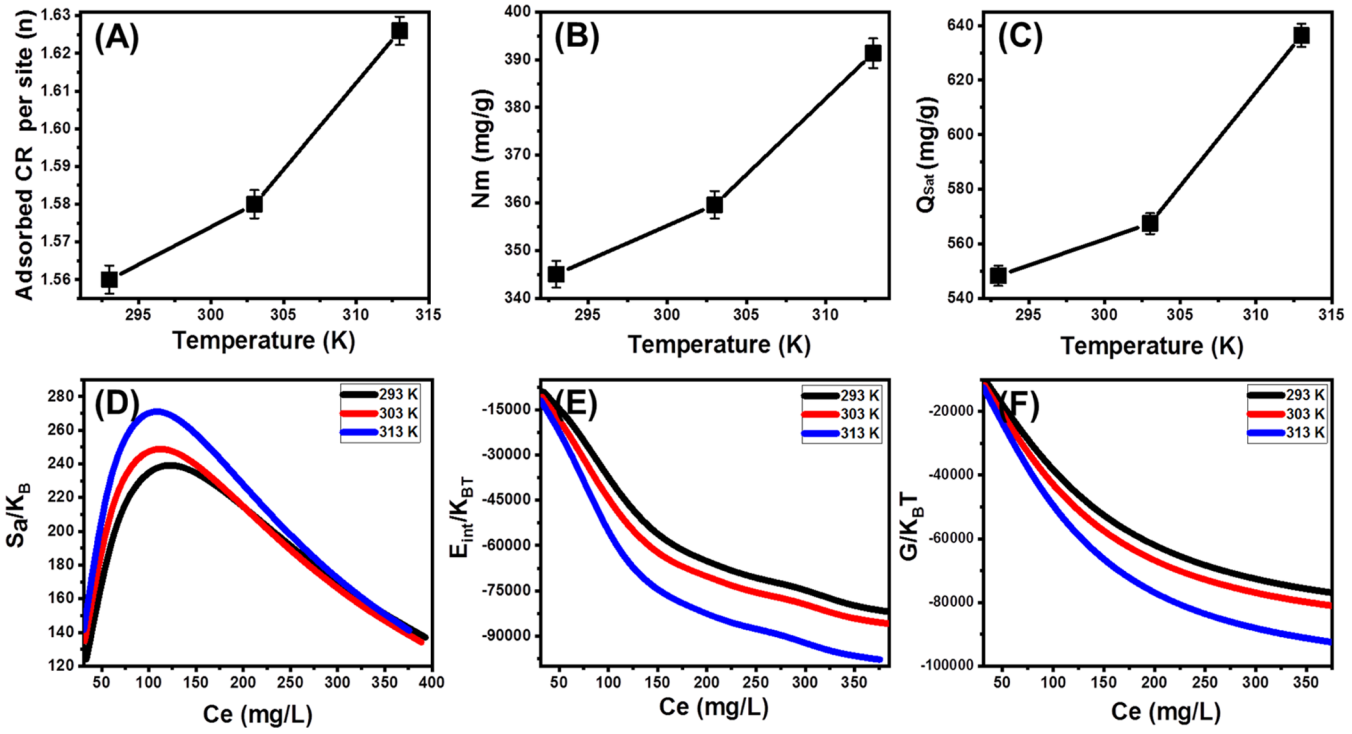

Figure 5. Change in the adsorbed CR molecules per each active site of Fe/GP with temperature (A), change in the active site density with temperature (B), change in the CR adsorption capacity as the saturation state with temperature (C), change in the entropy values with temperature and CR concentration (D), change in the internal energy with temperature and CR concentration (E), and change in the free enthalpy values with temperature and CR concentration (F).

Fe/GP is 5.8 and reflects the saturation of the Fe/GP surface with negative charges during CR adsorption at pH > 5.8; positive charges saturate the Fe/GP surface at pH < 5.8.

2.2.2. Equilibrium Studies. 2.2.2.1. Effect of CR Concentrations. The study of the Fe/GP adsorption capacity at different CR concentrations (50−500 mg/L) allows determining the actual maximum, or saturation capacity of the structure, and the equilibrium behavior of the CR adsorption on Fe/GP. The other variables were kept constant during the experiments [volume, 100 mL; solid dosage, 0.1 g/L; pH, 2; contact interval, 24 h]; the temperature effect was studied from 293 to 313 K (Figure 4B). The CR uptake by Fe/GP is notably enhanced when the CR concentration is high (Figure 4B). This enhancement is attributed to an increase in the diffusion speed and the driving forces of the CR molecules, which can increase their collision rates and interactions with the main effective receptors on the Fe/GP surface.[27] The increase in the CR adsorption efficiency is detected at all of the tested concentrations in the three equilibrium tests performed at 293, 303, and 313 K (Figure 4B). This concentration can be identified as the CR equilibrium concentration when Fe/GP is used as an adsorbent; the active sites that are present attain their saturation capacity with the adsorbed dye molecules; that is, they attain their maximum adsorption capacity. The CR equilibrium capacities of Fe/GP at the different temperatures are 535 mg/g (293 K), 558.2 mg/g (303 K), and 622 mg/g (313 K), indicating that the reactions are endothermic (Figure 4B).

2.2.2.2. Classic Isotherm Models. The equilibrium behavior of the CR adsorption on the Fe/GP particles was evaluated on the basis of the obtained nonlinear fitting degrees with the isotherm assumptions of the commonly studied classic equilibrium models, namely, the Langmuir (L.G) (Figure 4C), Freundlich (F.E) (Figure 4D), and Dubinin−Radushkevich (D−R) (Figure 4E) models; their fitting theoretical parameters (Table 1) were also evaluated. Upon consideration of the obtained values of R^2 and χ^2, it was concluded that the CR uptake by the Fe/GP particles followed the equilibrium properties of the Langmuir isotherm rather than the Freundlich isotherm at all of the inspected experimental temperatures (Table 1). This type of equilibrium behavior suggests the homogeneous adsorption of CR molecules on the surface of Fe/GP in a monolayer.[32] The theoretical maximum adsorbed quantities of CR by Fe/GP are 555.3, 575.9, and 644.12 mg/g at the studied temperatures of 293, 303, and 313 K, respectively (Table 1). The Gaussian energy values for the CR uptake by the Fe/GP particles are obtained as the mathematical fitting parameter for the D−R isotherm model. The estimated Gaussian energy values are 1.94 kJ/mol (293 K), 2.14 kJ/mol (303 K), and 2.15 kJ/mol (313 K). These values are within the reported energy range for physisorption mechanisms (<8 kJ/mol).

2.2.2.3. Advanced Isotherm Models. The advanced equilibrium model [monolayer model of one energy site (DL1)] was assessed to introduce more isotherm and mechanistic significance by considering the assumptions of the statistical physics theory. This model was selected based on the best-obtained values of RMSE and R^2 for the models, listed in Table S1 (Figure 4F; Table 1). The obtained mathematical fitting parameters of the DL1 model involve steric parameters [n (number of CR molecules per site), N_m (active density of a site of Fe/GP), and Q_{sat} (adsorption capacity of CR at the saturation state of Fe/GP)], and energetic parameters [ΔE (adsorption energy of CR), G (enthalpy), S_a (entropy), and E_{int} (internal energy)] (Table 1).

https://doi.org/10.1021/acsomega.2c03365
ACS Omega 2022, 7, 31218−31232

2.2.3. Steric Parameters. The number of adsorbed CR molecules per active uptake site (n parameter) of Fe/GP reflects the type of adsorption mechanism and the orientation properties of the adsorbed dye molecules (Figure 5A; Table 1). The values of the *n* parameter are 1.56 (293 K), 1.58 (303 K), and 1.62 (313 K), which are >1 (Figure 5A; Table 1). Therefore, one or two molecules of the CR dye are adsorbed on the surface of the Fe/GP particles via a multimolecular mechanism and are oriented in a nonparallel or vertical form.[33] The slight increase detected in the number of adsorbed CR molecules per site as a function of the tested temperature (293−313 K) demonstrates a slight or negligible enhancement of the aggregation properties of the CR molecules with an increase in temperature (Figure 5A).

The N_m parameter reflects the number of active adsorption sites on the surface of the used Fe/GP particles and considers the target dissolved chemicals. The estimated values from the fitting processes are 345.07 mg/g (293 K), 359.6 mg/g (303 K), and 391.37 mg/g (313 K) (Figure 5B; Table 1). This behavior suggests the considerable impact of the temperature on the activation of new adsorption sites or new energetic site groups.[33,34] This phenomenon occurs because an increase in the temperature decreases the viscosity of the dye solution and increases the diffusion rate and mobility of the dye within the pores of the geopolymer matrix, allowing complete contact with the additional active sites. Additionally, the high-temperature conditions improve the ion exchange properties of the geopolymer structure, the chemisorption reaction, and the formation of chemical bonds. The estimated adsorption capacity of CR at the saturation state (Q_{sat}) of the Fe/GP particles exhibits the same trend as those for the *n* and N_m parameters with a change in temperature, reflecting the controlling effect of the two parameters on the adsorption capacity of the geopolymer. The estimated values are 538.3 mg/g (293 K), 568.2 mg/g (303 K), and 634.02 mg/g (313 K) (Figure 5C; Table 1).

2.2.4. Energetic Parameters. 2.2.4.1. Adsorption Energy. The adsorption energy of the CR molecules by the Fe/GP particles is a strong indicator of the operating uptake mechanism. The CR adsorption energies at the studied temperature conditions were estimated on the basis of eq 1.[33]

$$\Delta E = RT \ln\left(\frac{S}{C}\right) \tag{1}$$

where ΔE, R, T, S, and C are the CR uptake energy, gas constant, absolute temperature, solubility of CR, and CR concentration at the half-saturation state of Fe/GP

The physical uptake mechanisms indicate adsorption energies of <40 kJ/mol and can be classified into five adsorption processes. These processes involve hydrogen bonding (<30 kJ/mol), van der Waals forces (4−10 kJ/mol), hydrophobic bonding (5 kJ/mol), coordination exchange processes (40 kJ/mol), and forces dipole bonding (2−29 kJ/mol).[33,35] The obtained energies for CR adsorption on Fe/GP (5.12−5.79 kJ/mol) reflect the physical uptake of the dye molecules by one or more processes, including hydrogen bonding, van der Waals forces, hydrophobic bonding, and forces dipole bonding (Table 1).

2.2.5. Thermodynamic Functions. 2.2.5.1. Entropy. The entropy, (S_a), as a thermodynamic function, signifies the disorder and order properties of the Fe/GP surface during the CR adsorption and considers the varying concentrations and temperature conditions. The entropy properties were evaluated based on the values obtained according to eq 2 considering the Boltzmann constant (k_B).[36]

$$\frac{S_a}{k_B} = N_m \left\{ \ln\left(1 + \left(\frac{C}{C_{1/2}}\right)^n\right) - n\left(\frac{C}{C_{1/2}}\right)^n \frac{\ln\left(\frac{C}{C_{1/2}}\right)}{1 + \left(\frac{C}{C_{1/2}}\right)^n} \right\} \tag{2}$$

The curves of S_a as a function of the CR concentration and temperature being evaluated show a noteworthy decrease as the dye concentration increases (Figure 5D). This behavior reflects a marked increase in the disordered properties of the Fe/GP surface during the CR uptake. Additionally, this result suggests notable docking of the CR molecules on the active sites of the Fe/GP structure when the reactions are performed at low dye concentrations.[36,37] The maximum values of entropy are observed at CR equilibrium concentrations of 119.9 mg/L (293 K), 114.7 mg/L (303 K), and 106.5 mg/L (313 K) and are close to those at the previously estimated CR concentrations at the half-saturation state of Fe/GP (C1/2) (Figure 5D). This result indicates that Fe/GP is saturated as an adsorbent for the CR molecules at these dye concentrations and no additional molecules can be docked on the active sites. Moreover, a decrease in the entropy values at higher concentrations suggests a marked decrease in the diffusion properties and degrees of freedom of the CR molecules, in addition to the availability of the active sites of the Fe/GP structure.[38]

2.2.5.2. Internal Energy and Free Enthalpy. The internal energy (E_{int}) of the CR adsorption on Fe/GP can be determined by eq 3, which considers the translation partition value (Z_v) and previously estimated steric parameters.[36]

$$\frac{E_{int}}{k_B T} = nN_m \left[\left(\frac{\left(\frac{C}{C_{1/2}}\right)^n \ln\left(\frac{C}{Z_v}\right)}{1 + \left(\frac{C}{C_{1/2}}\right)^n} \right) - \left(\frac{n \ln\left(\frac{C}{C_{1/2}}\right)\left(\frac{C}{C_{1/2}}\right)^n}{1 + \left(\frac{C}{C_{1/2}}\right)^n} \right) \right] \tag{3}$$

The obtained E_{int} values of the CR adsorption on Fe/GP are negative at the concentrations and temperatures studied and signify the spontaneity of the system (Figure 5E). The E_{int} values markedly increase when the test temperature increases from 293 to 313 K, which demonstrates that the CR uptake by Fe/GP is endothermic (Figure 5E). The free enthalpy (G) values determined using eq 4 considering the Boltzmann constant (k_B), and their behavior as a function of the dependent experimental conditions support, the internal energy findings (Figure 5F). The negative G values demonstrate the spontaneous uptake of the CR molecules by Fe/GP; the increase in the G values with an increase in temperature reflects the enhancement of the feasibility of these reactions.

$$\frac{G}{k_B T} = nN_m \frac{\ln\left(\frac{C}{Z_v}\right)}{1 + \left(\frac{C_{1/2}}{C}\right)^n} \tag{4}$$

2.3. Photo-Fenton Oxidation of CR. *2.3.1. Effect of Oxidation Parameters. 2.3.1.1. Effect of pH.* The impact of pH on the oxidation performance of Fe/GP as a heterogeneous catalyst in the photo-Fenton oxidation system was assessed over a pH range of 2−8, considering the existence of

https://doi.org/10.1021/acsomega.2c03365
ACS Omega 2022, 7, 31218−31232

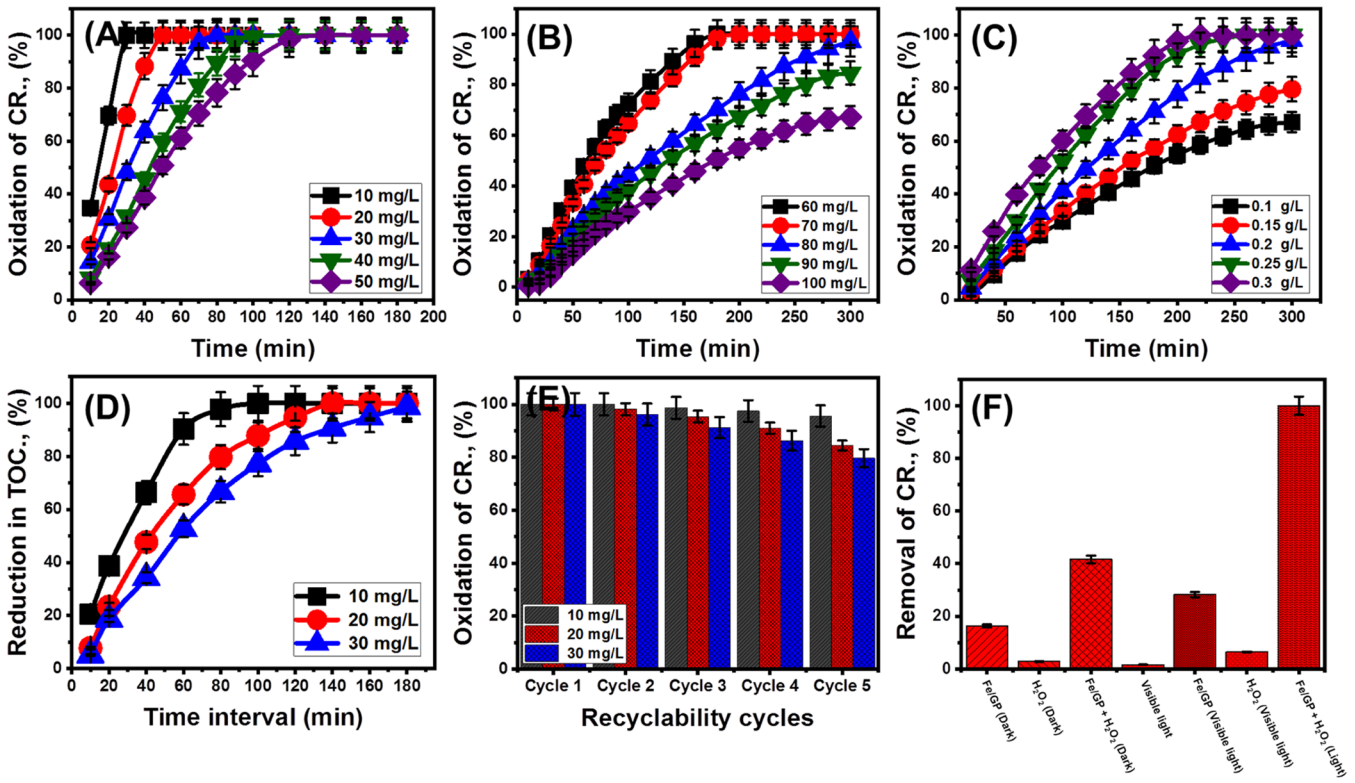

Figure 6. Advanced oxidation of low CR concentrations by Fe/GP at different intervals (A), advanced oxidation of high CR concentrations by Fe/GP at different intervals (B), advanced oxidation of CR dye by different dosages of Fe/GP at different intervals (C), reduction in the TOC content during the oxidation of CR dye (D), recyclability properties of Fe/GP catalyst (E), and synergetic effect of the different affecting factors during the oxidation of CR dye by Fe/GP (F).

the catalysts in their adsorption/desorption equilibrium state when 0.1 mL of H_2O_2 is used as an oxidizing activator. The other variables were kept constant during the experiments [volume, 100 mL; solid dosage, 0.1 g/L; concentration, 50 mg/L; oxidation interval, 120 min; temperature, 20 °C] (Figure S1). The oxidation results are reversible, as compared with the obtained adsorption results of CR as a function of the studied pH. The oxidation of CR by Fe/GP is enhanced markedly when the tests are performed under alkaline (98.3% at pH 8) conditions in relation to those performed under acidic conditions. This difference arises because the alkaline conditions induce the formation of surficial hydroxyl groups as the initiators of oxidizing radicals.[40] The formation of the hydroxyl groups is related to the noteworthy deprotonation of the active surface functional groups of Fe/GP.[3] These groups are commonly oxidized during the advanced oxidation of CR to oxidizing hydroxyl radicals. Moreover, the predicted overadsorption of the CR molecules under acidic conditions negatively affects the catalytic performance of Fe/GP because the direct interaction between the Fe/GP surface and the incorporated H_2O_2 or incident light photons is prevented.[40]

2.3.1.2. Effect of CR Concentrations at Different Oxidation Intervals. The catalytic performance of Fe/GP toward CR oxidation as a function of CR concentration was assessed under two conditions: low concentrations (10−50 mg/L) (Figure 6A) and high concentrations (60−100 mg/L) (Figure 6B) of CR. The other variables were kept constant during the experiments [volume, 100 mL; solid dosage, 0.1 g/L; H_2O_2 volume, 0.1 mL; temperature, 20 °C]. At low CR concentrations, the applied Fe/GP catalyst achieved noteworthy oxidation efficiencies within considerable time intervals (Figure 6A). Complete oxidation at the tested 10, 20, 30, 40, and 50 mg/L CR concentrations is achieved after 30, 50, 80, 120, and 140 min, respectively (Figure 6A). Identical high oxidation efficiencies are achieved at high CR concentrations (60 and 70 mg/L). The optimal oxidation efficiencies at CR concentrations of 80 mg/L (97.2%), 90 mg/L (84.6%), and 100 mg/L (67.2%) are observed after 300 min (Figure 6B).

The observed decline in the activity of Fe/GP at high CR concentrations may be related to the accumulation of a thick layer of adsorbed CR on the geopolymer surface. The formation of the adsorbed layer, in addition to the low light penetration properties, at high CR concentrations weakens the interaction between the light photons and the active catalytic sites of Fe/GP as well as that between the light photons and the H_2O_2 activator.[39] This weakened interaction, in turn, negatively affects the quantity of the produced oxidizing species and the rate of the Fenton oxidation reaction. The CR oxidation rate as a function of the tested intervals exhibits a detectable decrease until the re-establishment of the equilibrium, at which a fixed oxidation rate and no notable increment in the oxidation efficiency are achieved. This behavior is related to the continuous depletion of the existing oxidizing species during the degradation of CR over time until complete consumption occurs after a certain interval.[40]

2.3.1.3. Effect of Catalyst Dosage at Different Oxidation Intervals. The influence of the incorporated catalyst was evaluated from 0.1 g/L up to 0.3 g/L as an essential factor to enhance the performance of Fe/GP during the Fenton's oxidation of high CR concentrations (Figure 6C). The other variables were kept constant during the experiments [volume, 100 mL; CR concentration, 100 mg/L; H_2O_2 volume, 0.1 mL;

https://doi.org/10.1021/acsomega.2c03365
ACS Omega 2022, 7, 31218−31232

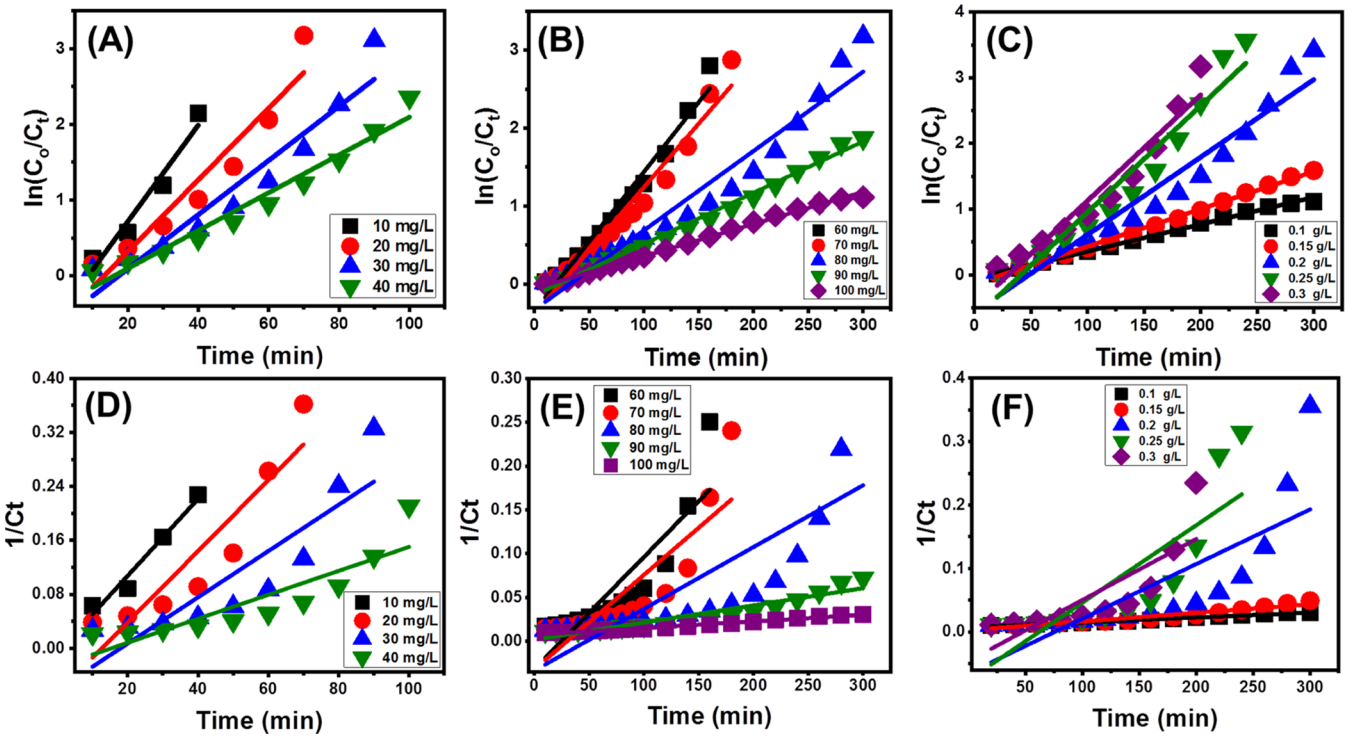

Figure 7. Fitting of the CR oxidation results with the first-order kinetic model at different experimental conditions (A−C) and fitting of the CR oxidation results with the second-order kinetic model at different experimental conditions (D−F).

temperature, 20 °C]. The profiles of CR oxidation as a function of Fe/GP dosage demonstrate a strong enhancement in the oxidation efficiency at high catalyst dosage (Figure 6C). This enhancement is mainly related to the marked increase in the number of catalytic sites present on the Fe/GP particle surfaces. This increase results in a notable increase in the interaction area between the CR molecules and the catalyst surface, in addition to a large increase in the number of generated oxidizing species.[41,42] The photo-Fenton oxidation at the studied CR concentration (100 mg/L) is completed after 260 min and 220 min using the Fe/GP catalyst at the adjusted dosages of 0.25 and 0.3 g/L, respectively (Figure 6C).

2.3.2. Mineralization Efficiency. The complete oxidation or degradation of the CR dye generates the end product of CO_2; therefore, the mineralization efficiency of the photo-Fenton oxidation of CR could be determined on the basis of the reduction in the TOC content of the treated samples. Three CR concentrations (10, 20, and 30 mg/L) were selected to determine the mineralization efficiency, considering the previously detected oxidation results (Figure 6D). The results indicate the complete removal of TOC from the treated CR solutions after 80 min (10 mg/L), 140 min (20 mg/L), and 180 min (30 mg/L) (Figure 6D). These findings demonstrate the complete mineralization of CR through the photo-Fenton oxidation reaction over Fe/GP, serving as a heterogeneous catalyst, after the previous intervals. The differences between the determined intervals for the complete oxidation and mineralization of CR demonstrate the existence of intermediate species. This hypothesis will be studied further, and future studies will consider the toxicities and structures of the intermediate species.

2.3.3. Recyclability. The recyclability and stability of Fe/GP as a heterogeneous catalyst during the photo-Fenton oxidation of CR are vital to expanding the commercial and practical application scope of the catalyst. After the oxidation tests, the spent Fe/GP was washed first with distilled water for four runs, and each run lasted 10 min. The spent Fe/GP was thereafter rinsed using a diluted NaOH solution (0.01 M) for 5 min. Subsequently, the Fe/GP fraction was washed again with distilled water until it reached its neutral state. Fe/GP was dried in an oven for 10 h at 75 °C for use in another cycle of the oxidation process. The recyclability tests were performed at three CR concentrations (10, 20, and 30 mg/L), and the other variables were kept constant during the experiments [volume, 100 mL; solid dosage, 0.1 g/L; oxidation interval, 100 min; H_2O_2 volume, 0.1 mL; temperature, 20 °C] (Figure 6E). The CR oxidation efficiency during the recyclability cycles (five runs) validated the stability and reusability of Fe/GP as catalysts for the photo-Fenton oxidation systems of synthetic dyes (Figure 6E). The oxidation efficiencies at 10 mg/L CR were 100% (cycle 1), 100% (cycle 2), 98.7% (cycle 3), 97.5% (cycle 4), and 95.6% (cycle 5) (Figure 6E). For the recyclability tests performed using 20 mg/L CR, the oxidation efficiencies were 100% (cycle 1), 98.2% (cycle 2), 95.4% (cycle 3), 91% (cycle 4), and 84.4% (cycle 5) (Figure 6E). For the tests using 30 mg/L CR, the oxidation efficiencies were 100% (cycle 1), 96.2% (cycle 2), 91.3% (cycle 3), 86.3% (cycle 4), and 79.7% (cycle 5) (Figure 6E). The previously determined oxidation efficiency during the recyclability of the Fe/GP catalyst can be significantly enhanced by extending the tested oxidation intervals or increasing the incorporated Fe/GP dosage.

2.3.4. Synergetic Properties of the Oxidation System. The impact of different components in the system for the photo-Fenton oxidation of CR over Fe/GP was determined by performing CR (50 mg/L) removal over Fe/GP under the following conditions:

- without a light source (adsorption)

https://doi.org/10.1021/acsomega.2c03365
ACS Omega 2022, 7, 31218−31232

Table 2. Estimated Correlation Coefficients, Kinetic Rate Constants, and Quantum Yields of the Occurred Oxidation Tests

		first order		second order		
		R^2	k_1	R^2	k_2	quantum yield (ϕ)
dosage	0. 1 g/L	0.99	0.0041	0.86	7.47×10^{-5}	1.266×10^{-9}
	0.15 g/L	0.99	0.0057	0.65	0.0473	1.761×10^{-9}
	0.2 g/L	0.93	0.0118	0.55	0.0590	3.707×10^{-9}
	0.25 g/L	0.93	0.0162	0.73	0.0662	5.406×10^{-9}
	0.3 g/L	0.93	0.0164	0.83	0.0861	5.468×10^{-9}
concentration	20 mg/L	0.95	0.063	0.93	0.0057	1.946×10^{-8}
	30 mg/L	0.90	0.047	0.82	0.0052	1.575×10^{-8}
	40 mg/L	0.91	0.035	0.75	0.0034	1.539×10^{-8}
	50 mg/L	0.95	0.025	0.74	0.0017	9.88×10^{-9}
	60 mg/L	0.97	0.0178	0.74	0.0012	5.87×10^{-9}
	70 mg/L	0.95	0.0162	0.71	0.0010	5.87×10^{-9}
	80 mg/L	0.94	0.0101	0.64	7.05×10^{-4}	3.08×10^{-9}
	90 mg/L	0.99	0.0065	0.89	1.95×10^{-4}	2.008×10^{-9}
	100 mg/L	0.99	0.0041	0.86	7.47×10^{-5}	1.266×10^{-9}

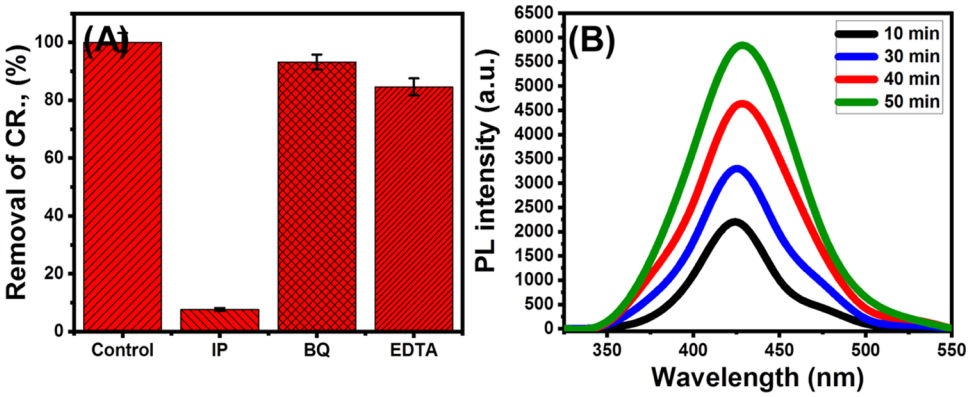

Figure 8. Results of the oxidizing species scavenging tests during oxidation of CR dye by Fe/GP (A) and the changes in the intensities of the PL spectra at different oxidation intervals (B).

- H_2O_2 (0.1 mL) without a light source
- Fe/GP + H_2O_2 (0.1 mL) without a light source (Fenton oxidation)
- visible light source
- Fe/GP in the presence of light sources (photocatalytic oxidation)
- H_2O_2 (0.1 mL) in the presence of a light source
- Fe/GP + H_2O_2 (0.1 mL) in the presence of a light source (photo-Fenton oxidation) (Figure 6F)

The tests were performed using the following experimental variables: volume, 100 mL; Fe/GP dosage, 0.1 g/L; removal interval, 120 min; CR concentration, 20 mg/L; and temperature, 20 °C.

Visible light has a slight or negligible effect on oxidation efficiency (1.6%); oxidation performed using H_2O_2 without a light source had a marginally greater impact than that using visible light (2.8%) in the absence of Fe/GP particles under the specified experimental conditions (Figure 6F). H_2O_2 exhibits a considerable oxidation effect in the presence of a light source (6.4%); the combination of H_2O_2 and Fe/GP particles results in a high oxidation efficiency without a light source (41.6%). These results validate the significant effect of the Fenton oxidation reactions on dye removal (Figure 6F).

When the Fe/GP catalyst is used in the presence of a light source (photocatalyst), there is a marked reduction in the CR oxidation efficiency (28.2%), while the combination of the Fe/GP particles, the light source, and H_2O_2 in the photo-Fenton oxidation system allows complete removal of CR at the studied concentration (50 mg/L). Therefore, the application of Fe/GP as a heterogeneous catalyst in the photo-Fenton oxidation toward CR dye removal is recommended instead of photocatalytic- or Fenton-oxidation-based removal.

2.3.5. Kinetic and Quantum Yield Studies. The kinetic behavior of the photo-Fenton oxidation of CR over the Fe/GP catalyst followed the assumptions of the first-order (eq 5) (Figure 7A–C) and second-order (eq 6) (Figure 7D–F) kinetic models considering the residual concentrations of CR after a certain time interval (C_t). The fitting degrees were considered on the basis of the obtained values of R^2 and χ^2 for the linear regression fitting processes using these models.

$$C_t = C_0\, e^{-k_1 t} \tag{5}$$

$$\frac{1}{C_t} = \frac{1}{C_0} + k_2 t \tag{6}$$

The fitting results demonstrate a good agreement between the results of the oxidation of CR at different concentrations and the kinetic properties of the first-order model; the results obtained as a function of Fe/GP dosage also show a better agreement with the kinetic properties of the first-order model (Table 2). Therefore, the oxidation reactions performed under these conditions appear to be controlled by only one of the experimental variables and mechanisms (oxidation interval, used dosage, or CR concentration). The increase in the value

https://doi.org/10.1021/acsomega.2c03365
ACS Omega 2022, 7, 31218–31232

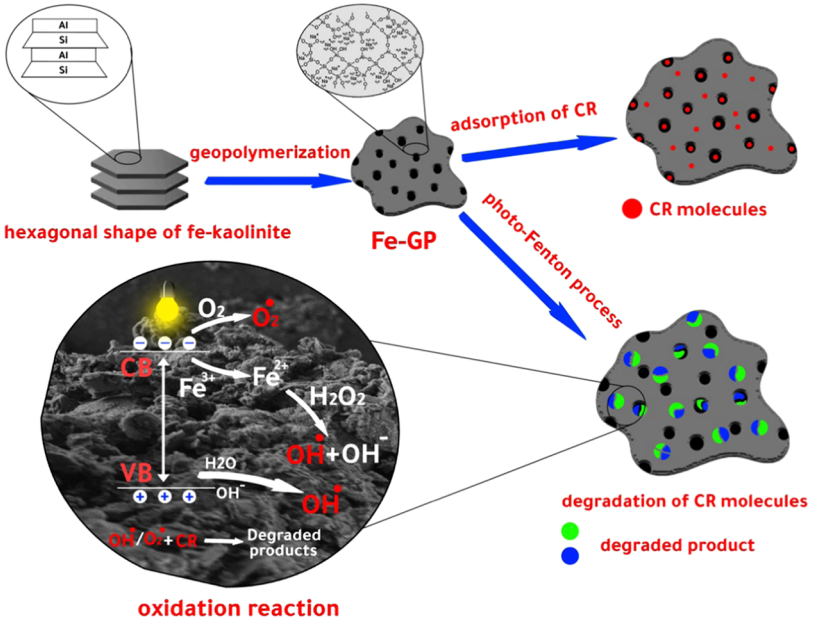

Figure 9. Schematic diagram for the synthesis of Fe/GP from Fe.K and its application in the oxidation of CR dye.

of the estimated kinetic rate constant with increasing Fe/GP dosage and its decrease with increasing CR concentration are in agreement with the experimental findings.

The detection of the quantum yield (ϕ) values for the photo-Fenton reactions reveals the impact of the studied experimental values on increasing or decreasing the efficiency of the process. The estimated ϕ values reflect the enrichment of the produced charge carriers that can achieve the highest oxidation efficiency for CR molecules per absorbed photon.[40] The apparent ϕ values for the tests were calculated on the basis of eq 7 using the estimated rate constant values of the first-order kinetics.

$$\Phi = \frac{k_1}{2.303 \times I_{o,\lambda} \times \varepsilon_\lambda \times l} \tag{7}$$

where k_1 is the first-order kinetic rate constant (S^{-1}), ε_λ is the molar absorptivity (cm^{-1} M^{-1}), $I_{o,\lambda}$ is the light intensity (Einstein I^{-1} S^{-1}), and l is the cell length (cm). The calculated ϕ values are in agreement with the experimental findings and indicate a possible enhancement in the efficiency of the CR oxidation upon increasing the Fe/GP dosage (Table 2).

2.3.6. Suggested Oxidation Mechanism. 2.3.6.1. Effective Oxidizing Species. The effective oxidizing species generated during photo-Fenton oxidation of CR over Fe/GP were identified as key factors that determine the oxidation pathway and mechanism. The identification was accomplished on the basis of a series of oxidizing species scavenging tests using isopropanol (IP), 1−4 benzoquinone (BQ), and EDTA-2Na (ED) as scavenging reagents (1 mmol) for hydroxyl radicals ($OH^{\bullet}$), superoxide radicals ($O_2^{\bullet-}$), and electron−hole pairs (h^+), respectively (Figure 8A). The oxidation efficiencies of CR (10 mg/L) in the presence of these reagents were reduced from 100% to 7.6% (IP), 93.2% (BQ), and 84.6% (ED) (Figure 8A). This result validates the essential effect of $OH^{\bullet}$ as a controlling oxidizing species during CR oxidation, followed by the assistive effect of the superoxide radicals ($O_2^{\bullet-}$).

The results of the oxidizing species scavenging tests were supported by the probe molecule detection of the generated hydroxyl radicals conducted using an experimental probe of terephthalic acid (5×10^{-4} M) (Figure 8B). The Fe/GP fractions were homogenized in a CR solution and a mixture of NaOH (2×10^{-3} M) and terephthalic acid. The quantities of the generated $OH^{\bullet}$ radicals were assessed on the basis of the quantities of hydroxyterephthalic acid produced during the chemical reactions between the $OH^{\bullet}$ radicals and probe molecules (terephthalic acid). The increase in the quantities of the hydroxyterephthalic acid produced during the oxidation reactions at different time intervals was assessed by photoluminescence spectroscopy (PL) conducted using a fluorescence spectrophotometer. The PL spectrum exhibits a marked increase in the peak intensity with increasing oxidation intervals (Figure 8B). These findings confirm that the $OH^{\bullet}$ radicals are the dominant oxidizing species during the photo-Fenton oxidation of CR over Fe/GP.

2.3.6.2. General Oxidation Mechanism. The oxidation of CR over Fe/GP, as a heterogeneous catalyst, occurred by the photo-Fenton reactions, following the mechanisms of the photocatalytic and Fenton oxidation processes. The initiation of both mechanisms involves the effective adsorption of the CR molecules on the active catalytic sites of Fe/GP and the production of the oxidizing species. During the photocatalytic process, the incident visible light photons induce the excitation of the outer electrons, which typically results in the formation of electron−hole pairs (h^+) (Figure 9).[43] The interaction of the migrated electrons with the oxygen ions results in the production of superoxide radicals ($O_2^{\bullet-}$).[43] Additionally, the formed electron−hole pairs (h^+) interact with water molecules, causing their splitting and the production of $OH^{\bullet}$ radicals.[44] All of the previously mentioned radicals are effectively utilized during the oxidation of the CR molecules, as summarized in eqs 8−14 (Figure 9).[45]

$$Fe/GP + h\nu \rightarrow Fe/GP(e_{CB}^-, h_{VB}^+) \tag{8}$$

$$Fe/GP(e^-) + O_2 \rightarrow Fe/GP + O_2^{\bullet-} \tag{9}$$

$$(Fe/GP)e^- + CR \rightarrow (Fe/GP)e^- + CR^{+\bullet} \tag{10}$$

$$CR^{+\bullet} + O_2^{\bullet-} \rightarrow \text{oxidized product} \tag{11}$$

https://doi.org/10.1021/acsomega.2c03365
ACS Omega 2022, 7, 31218−31232

Table 3. Comparison between the Adsorption and Catalytic Activities of Fe/GP and Other Studied Materials in the Literature

catalysts	dosage	conc.	light source	oxidation (%)	references
Ni−TiO_2	0.02 g/L	10 mg/L	450 W Xe lamp	180 min, ca.92.3%	14
CuO NPs	0.01 g/L	5×10^{-5} M	100 W electric bulb	120 min, ca. 91%	46
BE/CH@Co_3O_4	0.02 g/L	25 mg/L	visible light source	240 min, ca. 98.8%	9
ZBiSe-NPs	0.225 g/L	40 mg/L	UV-1602 double beam	120 min, ca. 99.6%	47
Cu_2O/ZnO	0.03 g/L	30 mg/L	300 W xenon lamp	10 min, ca. 100%	49
H_2O_2, Fe^{2+}	10 mg/L	50 mg/L	11 W UV lamp	120 min, ca. 94%	50
SnO_2−Fe_3O4	0.03 g/L	18 mg/L	14 W UV lamp	90 min, ca. 50.76%	51
TiO_2-$CoFe_2O_4$	0.08 g/L	100 mg/L	150 W metal halide lamp	250 min, ca. 97%	52
Fe/GP	0.1 g/L	10 mg/L	metal halide lamp, 0.1 mL H_2O_2	20 min, ca. 100%	this study
Fe/GP	0.1 g/L	20 mg/L	metal halide lamp, 0.1 mL H_2O_2	50 min, ca. 100%	this study
Fe/GP	0.1 g/L	30 mg/L	metal halide lamp, 0.1 mL H_2O_2	80 min, ca. 100%	this study
Fe/GP	0.1 g/L	40 mg/L	metal halide lamp, 0.1 mL H_2O_2	120 min, ca. 100%	this study
Fe/GP	0.1 g/L	50 mg/L	metal halide lamp, 0.1 mL H_2O_2	140 min, ca. 100%	this study
Fe/GP	0.1 g/L	60 mg/L	metal halide lamp, 0.1 mL H_2O_2	180 min, ca. 100%	this study
Fe/GP	0.1 g/L	70 mg/L	metal halide lamp, 0.1 mL H_2O_2	200 min, ca. 100%	this study
Fe/GP	0.3 g/L	100 mg/L	metal halide lamp, 0.1 mL H_2O_2	220 min, ca. 100%	this study

Adsorption

adsorbents	adsorption capacity (mg/g)	references
MNPs@NiFe LDH	79.6	53
MMO/Cs	3303	28
BE/CH@Co	303	9
Zn-MOF	355.16	54
polyacrolein (PA-1)	140.8	55
Fe_3O_4-OPBC-1 NCs	317.33	56
Fe_3O_4-OPBC-2 NCs	299.82	57
Fe_3O_4-PSP	216.9	
Fe/GP	634	this study

$$Fe/GP(h^+) + H_2O \rightarrow Fe/GP + H^+ \uparrow + OH^\bullet \quad (12)$$

$$Fe/GP(h^+) + CR \rightarrow \text{oxidized product} \quad (13)$$

$$CR + OH^\bullet \rightarrow \text{oxidized product} \rightarrow CO_2 + H_2O \quad (14)$$

During the Fenton oxidation process, the interaction between the migrated electrons and the H_2O_2 molecules, in addition to the photolysis effect, results in the production of hydroxyl groups OH^-, which are oxidized to $OH^\bullet$ oxidizing radicals by the electron−hole pairs (h^+). Additionally, the photogenerated or migrated electrons from the Fe/GP surface cause a reduction in the number of ferric ions (Fe(III)) present in the ferrous form (Fe(II)). The reaction between the resulting ferrous ions and H_2O_2, as an oxidizing reagent, results in the production of Fe(III) in addition to $OH^\bullet$ oxidizing radicals; the $OH^\bullet$ radicals generate ferrous iron forms by Fenton-like reactions in a continuous and regenerative process. All of the produced hydroxyl radicals induce the oxidation of the CR molecules to end products, as summarized in eqs 15−20 (Figure 9).

$$Fe/GP(e^-) + H_2O_2 \rightarrow OH^\bullet + OH^- \quad (15)$$

$$Fe/GP(h^+) + OH^- \rightarrow OH^\bullet \quad (16)$$

$$(Fe/GP)e^- + Fe^{3+} \rightarrow Fe^{2+} \quad (17)$$

$$Fe^{2+} + H_2O_2 \rightarrow OH^\bullet + Fe^{3+} + OH^- \quad (18)$$

$$Fe^{3+} + H_2O_2 \rightarrow HO_2^\bullet + Fe^{2+} + H^+ \quad (19)$$

$$CR + OH^\bullet \rightarrow \text{oxidized product} \rightarrow CO_2 + H_2O \quad (20)$$

2.3.7. Comparison Study. The efficiency of the synthetic Fe/GP as an adsorbent or a catalyst was compared with that of recently studied adsorbents and heterogeneous catalysts (Table 3). The presented results demonstrate a higher CR adsorption capacity of Fe/GP than those of other materials. Additionally, the reported catalytic activity toward CR oxidation reflects the higher oxidation efficiency of Fe/GP based on the estimated oxidation efficiency values, treated volumes, treated concentrations, and consumed time intervals. Because of the abovementioned technical advantages and commercial value of Fe/GP, which is achieved through low-cost, facile synthesis and using widely available precursors, Fe/GP can be more effectively used in practical applications, compared to most of the reported expensive catalysts.[48]

3. CONCLUSIONS

A modified form of an iron-impeded geopolymer (Fe/GP) was synthesized from ferruginous kaolinite. Its performance as an adsorbent of CR and as a catalyst for photo-Fenton oxidation was evaluated. Based on the monolayer equilibrium model of one energy, Fe/GP was found to possess an active adsorption site density of 391.3 mg/g, and each site can adsorb two dye molecules in a vertical orientation. These steric properties strongly induced an adsorption capacity of 634 mg/g, which is higher than those of numerous studied adsorbents. The results of energetic studies (5.12 to 5.7 kJ/mol) and thermodynamic functions (entropy, internal energy, and enthalpy) demonstrate that the adsorption mechanism of Fe/GP is exothermic and that it allows a spontaneous physisorption process. As a catalyst, Fe/GP exhibited high efficiency during the photo-Fenton oxidation of CR. Complete oxidation (100%) can be achieved at different CR concentrations (up to 100 mg/L)

https://doi.org/10.1021/acsomega.2c03365
ACS Omega 2022, 7, 31218−31232

within considerable intervals in the presence of 0.1 mL of H_2O_2 and a visible light source.

4. EXPERIMENTAL WORK

4.1. Materials. A natural ferruginous kaolinite sample was obtained from the Kalabsha kaolinite mine as a mining byproduct. The assessed samples were composed of Al_2O_3 (30.11%), SiO_2 (41.14%), Fe_2O_3 (12.5%), TiO_2 (2.74%), and L.O.I (11.4%) and trace quantities of MgO (0.21%), K_2O (0.24%), Na_2O (0.14%), and CaO (1.12%). Pellets of sodium hydroxide (El-Nasr Company; 97% purity) and optical glass solid waste with a 994% SiO_2 content were used during the synthesis. H_2O_2 (30% w/v) was used as the oxidizing reagent during the photo-Fenton oxidation studies. CR dye ($C_{32}H_{22}N_6Na_2O_6S_2$) powder was obtained from Sigma-Aldrich (Egypt) for use in the oxidation and adsorption tests.

4.2. Synthesis of the Iron-Impeded Geopolymer (Fe/GP). The synthesis steps were accomplished using the previously reported methodology.[3] First, a natural ferruginous kaolinite sample (Fe.K) was mechanically activated using a ball mill for approximately 2 h to reduce the size of the precursor particles to less than 100 μm. The ground Fe.K fractions were mixed homogenously with the sodium silicate pellets and optical glass solid waste to adjust the composition at the Si/Al ratio of the poly(sialate-siloxy) geopolymer. The three components were mixed with an alkaline solution of NaOH (12 M) for 5 h with continuous stirring at a fixed speed of 400 rpm. The obtained slurry was then modeled at 50 °C for 24 h, ground to achieve a size of 20−100 μm, and labeled as Fe/GP for further characterization.

4.3. Characterization. The crystalline properties were studied through X-ray diffraction (XRD) analysis conducted over 5°−70° by utilizing a PANalytical X-ray diffractometer (Empyrean). The surface features were investigated through scanning electron microscopy (SEM, Gemini, Zeiss-Ultra 55). SEM was performed after coating the products with a thin film of Au at an accelerating voltage of 5−30 kV. The chemical structure was assessed by Fourier transform infrared (FT-IR) spectroscopy of Fe.K and Fe/GP at wavenumbers ranging from 4000 to 400 cm^{-1} using a transform infrared spectrometer (FT-IR-8400S; Shimadzu). The elemental composition of the structures was evaluated by energy-dispersive X-ray (EDX) spectroscopy. The surface area and porous structure of Fe.K and Fe/GP were investigated using a surface area analyzer (Beckman Coulter SA3100). The ζ potential values of Fe/GP were measured at different pH values using a zetasizer system with a disposable ζ cell (Malvern, version 7.11) to determine pH at a zero-point charge ($pH_{(zpc)}$).

4.4. Batch Adsorption Studies of CR Dye. Batch uptake tests of the CR dye by Fe/GP were performed to detect the equilibrium properties of Fe/GP at different CR concentrations (50−500 mg/L) and three different temperatures (293, 303, and 313 K). The tests were completed while keeping the following variables constant: volume (100 mL), contact time (24 h), and dosage (0.1 g). The tests were repeated thrice, and the results were presented with a standard deviation of <5.3%. After the equilibrium period, the Fe/GP particles were extracted from the treated CR solutions, and the concentration of the remaining dye was determined using a UV−vis spectrophotometer. The concentrations of remaining CR were used to calculate the actual uptake capacity of Fe/GP, according to eq 21.

$$Q_e\ (\mathrm{mg/g}) = \frac{(C_o - C_e)V}{m} \tag{21}$$

where Q_e (mg/g), C_o (mg/L), C_e (mg/L), V (mL), and m (mg) are the CR uptake capacity, used CR concentration, remaining CR concentration, volume, and incorporated Fe/GP quantity, respectively. The nonlinear fitting of the CR uptake results achieved by the common classic isotherm models (Table S1) was accomplished on the basis of the estimated values of the correlation coefficient (R^2) (eq 22) and chi-square (χ^2) test (eq 23), where $q_{e,exp}$ and $q_{e,cal}$ are the experimental uptake capacity and the theoretical uptake capacity of CR, respectively.

$$R^2 = 1 - \frac{\sum (q_{e,exp} - q_{e,cal})^2}{\sum (q_{e,exp} - q_{e,mean})^2} \tag{22}$$

$$\chi^2 = \sum \frac{(q_{e,exp} - q_{e,cal})^2}{q_{e,cal}} \tag{23}$$

The nonlinear fitting of the advanced isotherm models based on statistical physics theory (Table S1) was considered on the basis of the R^2 and root-mean-square error (RMSE) from eq 24.

$$\mathrm{RMSE} = \frac{\sqrt{\sum_{i=1}^{m} (Q_{i,cal} - Q_{i,exp})^2}}{m' - p} \tag{24}$$

where m', p, $Q_{i,cal}$, and $Q_{i,exp}$ are the actually obtained results, studied experimental variables, theoretical CR uptake capacity, and actual CR uptake capacity, respectively.

4.5. Photo-Fenton Oxidation of CR Dye. The catalytic performance of Fe/GP as a heterogeneous catalyst for the photo-Fenton oxidation of the CR dye was assessed using a visible light source and H_2O_2 after reaching the adsorption/desorption equilibrium state. After the equilibration interval, as detected in the adsorption study, the stabilized Fe/GP particles were transferred to fresh CR solutions of varying concentrations to perform the oxidation tests without predicting the impact of the adsorption reactions. The light source was a visible light metal halide lamp (400 W) with an average wavelength and incident photon intensity of 490 nm and 18.7 mW/cm^2, respectively. The tests were conducted at varying concentrations of the CR dye at different oxidation intervals using different dosages of Fe/GP; the volume, solution pH, and temperature were kept constant at 100 mL, pH 8, and 20 °C, respectively. All of the oxidation tests were repeated thrice, considering the average values for all of the determining results with standard deviations of <5.6%. The oxidation percentage of the CR dye was calculated according to eq 25, which considers the predetermined remaining concentration of the dye after the absorbance tests. The mineralization efficiency was assessed by considering the decrease in the total organic content (TOC) of the treated CR samples using a TOC-VCPH (Shimadzu, Japan).

$$R\ (\%) = \frac{(C_o - C_e) \times 100}{C_o} \tag{25}$$

https://doi.org/10.1021/acsomega.2c03365
ACS Omega 2022, 7, 31218−31232

■ ASSOCIATED CONTENT

Supporting Information

The Supporting Information is available free of charge at https://pubs.acs.org/doi/10.1021/acsomega.2c03365.

Representative equations of the kinetic and isotherm models (Table S1) and the representative figure for the effect of pH values on the oxidation of CR by Fe/GP (Figure S1) (PDF)

■ AUTHOR INFORMATION

Corresponding Authors

Wail Al Zoubi − *Materials Electrochemistry Laboratory, School of Materials Science and Engineering, Yeungnam University, Gyeongsan 38541, Republic of Korea;* orcid.org/0000-0003-4213-8481; Email: Wailalzoubi@ynu.ac.kr

Mostafa R. Abukhadra − *Materials Technologies and Their Applications Lab, Geology Department, Faculty of Science, Beni-Suef University, Beni-Suef 65211, Egypt; Geology Department, Faculty of Science, Beni-Suef University, Beni-Suef 65211, Egypt;* orcid.org/0000-0001-5404-7996; Email: Abukhadra89@Science.bsu.edu.eg

Authors

Esraa R. Adly − *Materials Technologies and Their Applications Lab, Geology Department, Faculty of Science, Beni-Suef University, Beni-Suef 65211, Egypt; Geology Department, Faculty of Science, Beni-Suef University, Beni-Suef 65211, Egypt*

Mohamed S. Shaban − *Geology Department, Faculty of Science, New Valley University, Kharga 72713, Egypt;* orcid.org/0000-0002-4368-8269

Ahmed M. El-Sherbeeny − *Industrial Engineering Department, College of Engineering, King Saud University, Riyadh 11421, Saudi Arabia;* orcid.org/0000-0003-3559-6249

Complete contact information is available at: https://pubs.acs.org/10.1021/acsomega.2c03365

Author Contributions

This article was written through the contribution of all authors. All authors have given approval to the final version of the manuscript

Notes

The authors declare no competing financial interest.

■ ACKNOWLEDGMENTS

The authors extend their appreciation to King Saud University for funding this work through the Researchers Supporting Project (number RSP-2021/133).

■ REFERENCES

(1) Ren, W.; Wu, X.; Yang, J.; Luo, L.; Liang, S.; Yang, H. Water pollution characteristics of inflowing rivers under different land-use patterns in the Daye Lake basin: pollution mode and management suggestions. *Environ. Monit. Assess.* **2022**, *194*, No. 10.

(2) Siddique, M. A. B.; Islam, A. R. M. T.; Hossain, M. S.; Khan, R.; Akbor, M. A.; Hasanuzzaman, M.; et al. Multivariate statistics and entropy theory for irrigation water quality and entropy-weighted index development in a subtropical urban river, Bangladesh. *Enviro. Sci. Pollut. Res.* **2022**, *29*, 8577−8596.

(3) Al Zoubi, W.; Kamil, M. P.; Fatimah, S.; Nashrah, N.; Ko, Y. G. Recent advances in hybrid organic-inorganic materials with spatial architecture for state-of-the-art- applications. *Prog. Mater. Sci.* **2020**, *112*, No. 100663.

(4) Salam, M. A.; Mokhtar, M.; Albukhari, S. M.; Baamer, D. F.; Palmisano, L.; AlHammadi, A. A.; Abukhadra, M. R. Synthesis of zeolite/geopolymer composite for enhanced sequestration of phosphate (PO_4^{3-}) and ammonium (NH4+) ions; equilibrium properties and realistic study. *J. Environ. Manage.* **2021**, *300*, No. 113723.

(5) Benisha, R.; Amalanathan, M.; Aravind, M.; Mary, M. S. M.; Ahmad, A.; Tabassum, S.; et al. Catharanthus roseus leaf extract mediated Ag-MgO nanocatalyst for photocatalytic degradation of Congo red dye and their antibacterial activity. *J. Mol. Struct.* **2022**, *1262*, No. 133005.

(6) Kumar Prajapati, A.; Mondal, M. K. Green synthesis of Fe_3O_4-onion peel biochar nanocomposites for adsorption of Cr (VI), methylene blue and congo red dye from aqueous solutions. *J. Mol. Liq.* **2022**, *349*, No. 118161.

(7) Taher, T.; Putra, R.; Palapa, N. R.; Lesbani, A. Preparation of magnetite-nanoparticle-decorated NiFe layered double hydroxide and its adsorption performance for congo red dye removal. *Chem. Phys. Lett.* **2021**, *777*, No. 138712.

(8) Lei, H.; Muhammad, Y.; Wang, K.; Yi, M.; He, C.; Wei, Y.; Fujita, T. Facile fabrication of metakaolin/slag-based zeolite microspheres (M/SZMs) geopolymer for the efficient remediation of Cs^+ and Sr^{2+} from aqueous media. *J. Hazard. Mater.* **2021**, *406*, No. 124292.

(9) Abukhadra, M. R.; Adlii, A.; Bakry, B. M. Green fabrication of bentonite/chitosan@cobalt oxide composite (BE/CH@Co) of enhanced adsorption and advanced oxidation removal of Congo red dye and Cr (VI) from water. *Int. J. Biol. Macromol.* **2019**, *126*, 402−413.

(10) Refat, M. S.; Saad, H. A.; Gobouri, A. A.; Alsawat, M.; Adam, A. M. A.; El-Megharbel, S. M. Charge transfer complexation between some transition metal ions with azo Schiff base donor as a smart precursor for synthesis of nano oxides: An adsorption efficiency for treatment of Congo red dye in wastewater. *J. Mol. Liq.* **2022**, *345*, No. 117140.

(11) Al Zoubi, W.; Nashrah, N.; Putri, R. A. K.; Allaf, A. W.; Assfour, B.; Ko, Y. G. Strong dual-metal-support interactions induced by low-temperature plasma phenomenon. *Mater. Today Nano* **2022**, *18*, No. 100213.

(12) Masalvad, S. K. S.; Sakare, P. K. Application of photo Fenton process for treatment of textile Congo-red dye solution. *Mater. Today: Proc.* **2021**, *46*, 5291−5297.

(13) Al Zoubi, W.; Allaf, A. W.; Assfour, B.; Ko, Y. G. Concurrent oxidation-reduction reactions in a single system using a low-plasma phenomenon: excellent catalytic performance and stability in hydrogenation reaction. *ACS Appl. Mater. Interfaces* **2022**, *14*, 6740−6753.

(14) Indira, K.; Shanmugam, S.; Hari, A.; Vasantharaj, S.; Sathiyavimal, S.; Brindhadevi, K.; et al. Photocatalytic degradation of congo red dye using nickel−titanium dioxide nanoflakes synthesized by Mukia madrasapatna leaf extract. *Environ. Res.* **2021**, *202*, No. 111627.

(15) Xiang, D.; Lu, S.; Ma, Y.; Zhao, L. Synergistic Photocatalysis-Fenton Reaction of Flower-shaped CeO_2/Fe_3O_4 Magnetic Catalyst for Decolorization of High Concentration Congo Red Dye. *Colloids Surf., A* **2022**, *647*, No. 129021.

(16) Cui, H.; Yu, J.; Zhu, X.; Cui, Y.; Ji, C.; Zhang, C.; et al. Advanced treatment of chicken farm flushing wastewater by integrating Fenton oxidation and algal cultivation process for algal growth and nutrients removal. *J. Environ. Manag.* **2021**, *298*, No. 113543.

(17) Yang, X.; Wang, J.; El-Sherbeeny, A. M.; AlHammadi, A. A.; Park, W. H.; Abukhadra, M. R. Insight into the adsorption and oxidation activity of a ZnO/piezoelectric quartz core-shell for

enhanced decontamination of ibuprofen: Steric, energetic, and oxidation studies. *Chem. Eng. J.* **2022**, *431*, No. 134312.
(18) Spector, P. E.; Fox, S.; Penney, L. M.; Bruursema, K.; Goh, A.; Kessler, S. The dimensionality of counterproductivity: Are all counterproductive behaviors created equal. *J. Vocat. Behav.* **2006**, *68*, 446.
(19) Al Zoubi, W.; Allaf, A. W.; Assfour, B.; Ko, Y. G. Toward two-dimensional hybrid organic-inorganic materials based on a I-PE/UHV-PVD system for exceptional corrosion protection. *Appl. Mater. Today.* **2021**, *24*, No. 1001142.
(20) Zhang, P.; Gao, Z.; Wang, J.; Guo, J.; Hu, S.; Ling, Y. Properties of fresh and hardened fly ash/slag based geopolymer concrete: A review. *J. Cleaner Prod.* **2020**, *270*, No. 122389.
(21) El-Sayed, T. A.; Shaheen, Y.B.I. Flexural performance of recycled wheat straw ash-based geopolymer RC beams and containing recycled steel fiber. *Structures* **2020**, *28*, 1713−1728.
(22) Rossatto, D. L.; Netto, M. S.; Jahn, S. L.; Mallmann, E. S.; Dotto, G. L.; Foletto, E. L. Highly efficient adsorption performance of a novel magnetic geopolymer/Fe_3O_4 composite towards removal of aqueous acid green 16 dye. *J. Environ. Chem. Eng.* **2020**, *8*, No. 103804.
(23) Giovanella, P.; Vieira, G. A.; Otero, I. V. R.; Pellizzer, E. P.; de Jesus Fontes, B.; Sette, L. D. Metal and organic pollutants bioremediation by extremophile microorganisms. *J. Hazard. Mater.* **2020**, *382*, No. 121024.
(24) Sithole, N.; Okonta, F.; Ntuli, F. Mechanical properties and structure of fly ash modified basic oxygen furnace slag based geopolymer masonry blocks. *J. Solid Waste Technol. Manage.* **2020**, *46*, 372−383.
(25) Shehata, N.; Mohamed, O. A.; Sayed, E. T.; Abdelkareem, M. A.; Olabi, A. G. Geopolymer concrete as green building materials: Recent applications, sustainable development and circular economy potentials. *Sci. Total Environ* **2022**, *836*, No. 155577.
(26) Shaban, M.; Sayed, M. I.; Shahien, M. G.; Abukhadra, M. R.; Ahmed, Z. M. Adsorption behavior of inorganic-and organic-modified kaolinite for Congo red dye from water, kinetic modeling, and equilibrium studies. *J. Sol-Gel Sci. Technol.* **2018**, *87*, 427−441.
(27) Salam, M. A.; Mokhtar, M.; Albukhari, S. M.; Baamer, D. F.; Palmisano, L.; Abukhadra, M. R. Insight into the role of the zeolitization process in enhancing the adsorption performance of kaolinite/diatomite geopolymer for effective retention of Sr (II) ions; batch and column studies. *J. Environ. Manag.* **2021**, *294*, No. 112984.
(28) Al Zoubi, W.; Khan, M. E.; Ko, Y. G. A simple method to functionalize the surface of plamsa electrolysis produced inorganic coatings for growing different organic structure. *Prog. Org. Coat.* **2022**, *171*, No. 107008.
(29) Gao, H.; Liu, H.; Liao, L.; Mei, L.; Zhang, F.; Zhang, L.; et al. A bifunctional hierarchical porous kaolinite geopolymer with good performance in thermal and sound insulation. *Constr. Build. Mater.* **2020**, *251*, No. 118888.
(30) Tran, T. N.; Do, Q. C.; Kim, D.; Kim, J.; Kang, S. Urchin-like structured magnetic hydroxyapatite for the selective separation of cerium ions from aqueous solutions. *J. Hazard. Mater.* **2022**, *430*, No. 128488.
(31) Abukhadra, M. R.; Dardir, F. M.; Shaban, M.; Ahmed, E. A.; Soliman, M. F. Superior removal of Co^{2+}, Cu^{2+} and Zn^{2+} contaminants from water utilizing spongy Ni/Fe carbonate−fluorapatite; preparation, application and mechanism. *Ecotoxicol. Environ. Saf.* **2018**, *157*, 358−368.
(32) El-Zeiny, H. M.; Abukhadra, M. R.; Sayed, O. M.; Osman, A. H.; Ahmed, S. A. Insight into novel β-cyclodextrin-grafted-poly (N-vinylcaprolactam) nanogel structures as advanced carriers for 5-fluorouracil: Equilibrium behavior and pharmacokinetic modeling. *Colloids Surf., A* **2020**, *586*, No. 124197.
(33) Dhaouadi, F.; Sellaoui, L.; Badawi, M.; Reynel-Ávila, H. E.; Mendoza-Castillo, D. I.; Jaime-Leal, J. E.; et al. Statistical physics interpretation of the adsorption mechanism of Pb^{2+}, Cd^{2+} and Ni^{2+} on chicken feathers. *J. Mol. Liq.* **2020**, *319*, No. 114168.
(34) Al Zoubi, W.; Putri, R. A. K.; Sunghun, B.; Ko, Y. G. Molecular structures in the inorganic-metal interactions for optimizing electrochemical performance. *J. Mol. Liq.* **2021**, *326*, No. 115344.
(35) Ali, R. A. M.; Mobarak, M.; Badawy, A. M.; Lima, E. C.; Seliem, M. K.; Ramadan, H. S. New insights into the surface oxidation role in enhancing Congo red dye uptake by Egyptian ilmenite ore: Experiments and physicochemical interpretations. *Surf. Interfaces* **2021**, *26*, No. 101316.
(36) Dhaouadi, F.; Sellaoui, L.; Reynel-Ávila, H. E.; Landín-Sandoval, V.; Mendoza-Castillo, D. I.; Jaime-Leal, J. E.; et al. Adsorption mechanism of Zn^{2+}, Ni^{2+}, Cd^{2+}, and Cu^{2+} ions by carbon-based adsorbents: interpretation of the adsorption isotherms via physical modelling. *Environ. Sci. Pollut. Res.* **2021**, *28*, 30943−30954.
(37) Al Zoubi, W.; Kim, M. J.; l Kim, Y. G.; Ko, Y. G. Enhanced chemical stability and boosted photoactivity by transition metal doped-crosslinked polymer-inorganic materials. *J. Mol. Liq.* **2020**, *303*, No. 112700.
(38) Sellaoui, L.; Guedidi, H.; SarraWjihi, S.; Reinert, L.; Reinert, L.; Knani, S.; Duclaux, L.; Lamine, A. B. Experimental and theoretical studies of adsorption of ibuprofen on raw and two chemically modified activated carbons: new physicochemical interpretations. *RSC Adv.* **2016**, *6*, 12363−12373.
(39) Abdullah, R. R.; Shabeed, K. M.; Alzubaydi, A. B.; Alsalhy, Q. F. Novel photocatalytic polyether sulphone ultrafiltration (UF) membrane reinforced with oxygen-deficient Tungsten Oxide (WO_2. 89) for Congo red dye removal. *Chem. Eng. Res. Des.* **2022**, *177*, 526−540.
(40) Wang, S.; Wang, F.; Jin, Y.; Meng, X.; Meng, B.; Yang, N.; et al. Removal of heavy metal cations and co-existing anions in simulated wastewater by two separated hydroxylated MXene membranes under an external voltage. *J. Membr. Sci.* **2021**, *638*, No. 119697.
(41) Abukhadra, M. R.; Othman, S. I.; Allam, A. A.; Elfayoumi, H. Insight into the catalytic properties zeolitized kaolinite/diatomite geopolymer as an environmental catalyst for the sustainable conversion of spent cooking oil into biodiesel; optimization and kinetics. *Sustainable Chem. Pharm.* **2021**, *22*, No. 100473.
(42) Al Zoubi, W.; Yoon, D. K.; Kim, Y. G.; Ko, Y. G. Fabrication of organic-inorganic hybrid materials on metal surface for optimizing electrochemical performance. *J. Colloid Interface Sci.* **2020**, *573*, 31−44.
(43) Zhang, Y.; Zhang, B. T.; Teng, Y.; Zhao, J.; Sun, X. Heterogeneous activation of persulfate by carbon nanofiber supported Fe_3O_4@ carbon composites for efficient ibuprofen degradation. *J. Hazard. Mater.* **2021**, *401*, No. 123428.
(44) Fard, S. G.; Haghighi, M.; Shabani, M. Facile one-pot ultrasound-assisted solvothermal fabrication of ball-flowerlike nanostructured (BiOBr) x ($Bi_7O_9I_3$) 1-x solid-solution for high active photodegradation of antibiotic levofloxacin under sun-light. *Appl. Catal., B* **2019**, *248*, 320−331.
(45) Sun, Q.; Hu, X.; Zheng, S.; Zhang, J.; Sheng, J. Effect of calcination on structure and photocatalytic property of NTiO_2/g-C_3N_4@diatomite hybrid photocatalyst for improving reduction of Cr(VI). *Environ. Pollut.* **2019**, *245*, 53−62.
(46) Alsamhary, K.; Al-Enazi, N. M.; Alhomaidi, E.; Alwakeel, S. Spirulina platensis mediated biosynthesis of Cuo Nps and photocatalytic degradation of toxic azo dye Congo red and kinetic studies. *Environ. Res.* **2022**, *207*, No. 112172.
(47) Khan, S.; Khan, A.; Ali, N.; Ahmad, S.; Ahmad, W.; Malik, S.; et al. Degradation of Congo red dye using ternary metal selenide-chitosan microspheres as robust and reusable catalysts. *Environ. Technol. Innovation* **2021**, *22*, No. 101402.
(48) Xiang, D.; Lu, S.; Ma, Y.; Zhao, L. Synergistic photocatalysis-fenton reaction of flower-shaped CeO2/Fe3O4 magnetic catalyst for decolorization of high concentration congo red dye. *Colloids Surf., A* **2022**, *647*, No. 129021.
(49) Mohammed, A. M.; Mohtar, S. S.; Aziz, F.; Aziz, M.; Ul-Hamid, A.; Wan Salleh, W. N.; et al. Ultrafast degradation of Congo Red dye using a facile one-pot solvothermal synthesis of cuprous oxide/titanium dioxide and cuprous oxide/zinc oxide p-n heterojunction photocatalyst. *Mater. Sci. Semicond. Process.* **2021**, *122*, No. 105481.

https://doi.org/10.1021/acsomega.2c03365
ACS Omega 2022, 7, 31218−31232

(50) Masalvad, S. K. S.; Kumar Sakare, P. Application of photo Fenton process for treatment of textile Congo-red dye solution. *Mater. Today: Proc.* **2021**, *46*, 5291−5297.
(51) Said, M.; Rizki, W. T.; Asri, W. R.; Desnelli, D.; Rachmat, A.; Hariani, P. L. SnO2−Fe3O4 nanocomposites for the photo-degradation of the Congo red dye. *Heliyon 8*, e09204. DOI: 10.1016/j.heliyon.2022.e09204.
(52) Al Zoubi, W.; Kim, M. J.; Kim, Y. G.; Ko, Y. G. Dual-functional crosslinked polymer-inorganic materials for robust electrochemical performance and antibacterial activity. *Chem. Eng. J.* **2020**, *392*, No. 123654.
(53) Taher, T.; Putra, R.; Rahayu Palapa, N.; Lesbani, A. Preparation of magnetite-nanoparticle-decorated NiFe layered double hydroxide and its adsorption performance for congo red dye removal. *Chem. Phys. Lett.* **2021**, *777*, No. 138712.
(54) Gao, L.; Gao, T.; Zhang, Y.; Hu, T. A bifunctional 3D porous Zn-MOF: Fluorescence recognition of Fe^{3+} and adsorption of congo red/methyl orange dyes in aqueous medium. *Dyes Pigm.* **2022**, *197*, No. 109945.
(55) Li, Y.; Tang, J.; Liu, Y.; Xiao, Z.; Zhang, Y. F. Concentration-driven selective adsorption of Congo red in binary dyes solution using polyacrolein: Experiments, characterization and mechanism studies. *J. Mol. Liq.* **2021**, *335*, No. 116230.
(56) Sayed, I. R.; Farhan, A. M.; Alhammadi; El-Sayed, M.; Abd El-Gaied, I. M.; El-Sherbeeny, A. M.; Al Zoubi, W.; Ko, Y. G.; Abukhadra, M. R. Synthesis of novel nanoporous zinc phosphate/hydroxyapatite nano-rods (ZPh/HPA_{NRs}) core/shell for enhanced adsorption of Ni^{2+} and Co^{2+} ions: characterization and application. *J. Mol. Liq.* **2022**, *360*, No. 119527.
(57) Al Zoubi, W.; Nashrah, N.; Chaouiki, A.; Ko, Y. G. Self-assembled molecular network formed by controlling molecular deposition of organic compounds. *FlatChem* **2021**, *29*, No. 100270.

https://doi.org/10.1021/acsomega.2c03365
ACS Omega 2022, 7, 31218−31232